Communications Materials

https://doi.org/10.1038/s43246-026-01228-4

Article in Press

The role of adhesion in triboelectrification trends of charge polarity and magnitude

Received: 1 December 2025

Accepted: 4 June 2026

Cite this article as: Ģērmane, L., Lapčinskis, L., Xu, T. *et al.* The role of adhesion in triboelectrification trends of charge polarity and magnitude. *Commun Mater* (2026). https://doi.org/10.1038/s43246-026-01228-4

Līva Ģērmane, Linards Lapčinskis, Tianhuai Xu, Jiahao Ye, Jēkabs Grušs, Andrea Le Donne, Hermanis Sorokins, Jin-Chong Tan & Andris Šutka

The Role of Adhesion in Triboelectrification Trends of Charge Polarity and Magnitude

Līva Ģērmane[1], Linards Lapčinskis[1], Tianhuai Xu[3], Jiahao Ye[3], Jēkabs Grušs[1], Andrea Le Donne[1], Hermanis Sorokins[2], Jin-Chong Tan[3]*, Andris Šutka[1]*

[1] Institute of Physics and Materials Science, Faculty of Natural Sciences and Technology, Riga Technical University, P. Valdena Street 3/7, Riga, LV-1048, Latvia

[2] Institute of Mechanical and Biomedical Engineering, Faculty of Civil and Mechanical Engineering, Riga Technical University, 6A Kipsalas Street, Riga, LV-1048, Latvia

[3] Multifunctional Materials & Composites (MMC) Laboratory, Department of Engineering Science, University of Oxford, Parks Road, Oxford, OX1 3PJ, UK

* jin-chong.tan@eng.ox.ac.uk

* andris.sutka@rtu.lv

Abstract

Triboelectricity – the generation of charge through the contact-separation – underpins technologies including energy harvesting and sensing. While the charge magnitude is known to depend on surface chemistry, morphology, and mechanical properties, the role of adhesion – particularly on charge polarity – remains unclear. Here, we investigate adhesion effects using polydimethylsiloxane (PDMS) films with different base polymer to curing agent ratios (5:1, 10:1, and 15:1), yielding distinct viscoelastic and adhesive properties without altering chemical structure. Nanoindentation and pull-off tests revealed that reduced cross-linking enhances viscoelastic deformation and work of adhesion. Triboelectric measurements demonstrated that more adhesive PDMS surfaces generate more negative charge densities. When PDMS films of differing adhesion were contacted, the more adhesive surface charged negatively, while the less adhesive one positively, enabling polarity control without chemical modifications. Increased contact duration further enhances both adhesion and charge density. These findings reveal that adhesion engineering, offers a simple strategy for optimizing triboelectric charging trends.

Introduction

Triboelectricity is a well-known phenomenon widely observed in daily life. The triboelectric charge manifests as static electricity on the surface of an insulating material. It occurs when materials such as non-conductive polymers are contacted and separated due to mechanical friction and surface adhesion effects. The triboelectric charge has both negative and positive effects. On the one hand, it causes the ignition and damage of electronic devices, but on the other hand, it provides a large variety of applications such as particle separation[1], waste mechanical energy harvesting[2], printing[3], sensing[4], and catalysis[5].

Higher surface charge densities are empirically observed when materials with differing apparent triboelectric charging tendencies undergo contact and separation interaction. While pairing a material that tends to charge positively with a polymer that tends to charge negatively according to the triboelectric series often results in increased charge output, however this behaviour represents a general trend not a rule. The triboelectric series itself is not a fundamental material ranking but is derived from experimental observations and is sensitive to testing conditions. Recent studies have shown that the magnitude and polarity of triboelectric charge depend on the polymer's mechanical properties, morphology, and adhesion[6-8]. For instance, experiments involving 196 polymer combinations revealed that softer materials tend to acquire a negative charge, while harder materials gain a positive charge[7]. Similarly, when chemically identical polymers are tested, rough surfaces typically charge positively, and smooth surfaces charge negatively[6,9]. Notably, stronger charging occurs when a soft, smooth polymer contacts a hard, rough polymer[6]. Here we will report the effect of adhesion on the polarity of triboelectric surface charge by contacting chemically identical polydimethylsiloxane (PDMS) films with different cross-linking densities.

Several studies have reported the effect of adhesion on triboelectric charging. Ghori et al.[10] discovered that increasing the proportion between hydroxyl and alkyl or silane groups on the cellulose surface led to a significant reduction in both the electrostatic charge and surface adhesion. Additionally, a direct linear relationship was observed between triboelectric charge and particle surface adhesion. Further, surface adhesion has been suggested as a driving force for heterolytic bond cleavage and mechano-ion (organoion) transfer[11]. The energy associated with this separation is most accurately characterized by the work of adhesion, which defines the energy required to detach two contacted polymer surfaces[12,13].

The adhesion effect can be tuned chemically, by changing the cross-linking degree of the polymer. Maeda et al.[14] found that cross-linked polymers exhibit lower adhesion compared to uncross-linked ones. This reduction is attributed to the restricted mobility of macromolecular chains, which limits their ability to form strong intermolecular bonding at the surface. Adjusting the cross-linking density can thus be an effective strategy for controlling polymer adhesion. Sutka et al. showed that the lower cross-linking density of PDMS increased the separation stress at contact interface from 1.0 N cm^{-2} to 3.4 N cm^{-2} (10-34 kPa) and surface charge density from 0.31 to 3.39 nC cm^{-2} [15].

Recent developments in triboelectric research have further expanded the field by showing that charge generation is not governed solely by solid–solid contact, but also by ion dynamics within the electrical double layer at solid–liquid interfaces. Dynamic control of the electrical double layer has enabled new triboiontronic concepts, including direct current triboiontronic nanogenerators, asymmetric double-layer formation, and Maxwell-demon-like ionic regulation. These studies demonstrate that triboelectric output is strongly influenced by ionic migration, Stern-layer polarization, and diffuse-layer modulation at dielectric–liquid interfaces, revealing that nanoscale interfacial processes can dramatically alter macroscopic charge behaviour[16-19]. This broader perspective underscores the importance of understanding how intrinsic material properties such as

adhesion influence not only charge density but also charge polarity, even when the polymer chemistry remains identical.

However, despite extensive research on how adhesion affects triboelectric surface charge density, the effect of surface stickiness on charge polarity remains unexplored. The existing research related to the effect of adhesion on polymer triboelectrification focuses on different material pairings, introducing several variables into the system such as distinct chemical composition[8], hydrophilicity[20] or zeta-potential[21]. Therefore, in this work we explore the impact of adhesion on charge polarity in the same polymer by contacting chemically identical PDMS with different degrees of molecular cross-linking.

Results and Discussion

The surface properties of PDMS samples

To alter the surface adhesion, the samples with different degrees of cross-linking were prepared by changing the ratio between the base polymer and a curing agent (CA), as illustrated in Figure 1 (A). Three different base polymer and CA ratios were chosen: 5:1, 10:1, and 15:1. Smaller ratio provides sample brittleness while larger ratio results in an incomplete cross-linking[22,23]. The different formulations change the molecular weight between cross-links (Table 1). The determined crosslink densities ρ_K decrease with increasing ratio of base agent to CA.

Dynamic mechanical analysis (DMA) using the nanoindenter probe provided information about the viscoelastic properties of the samples across a range of frequencies (Figure 1), such as stiffness, energy dissipation, and molecular mobility. Both the storage modulus (E') and loss modulus (E") decreased with reduced cross-linking, reflecting less stiffness and damping capacity in softer composition[24,25]. The most cross-linked composition exhibited the highest moduli, consistent with its lower deformation and higher resistance to detachment observed[26]. For 10:1 and 15:1 compositions, loss tangent values were relatively similar at low frequencies; however, at higher frequencies, the 15:1 composition showed a slight increase in loss tangent. This suggests enhanced energy dissipation in dynamic conditions, likely due its greater molecular mobility and viscoelastic damping, which may further contribute to the increased work of adhesion observed despite lower pull-off forces (Table 1). The dynamic mechanical analysis provided direct evidence for the changes of mechanical properties resulting from variations in cross-linking. This confirms that deviations from the standard formulation significantly influence the viscoelastic behaviour, stiffness, and energy dissipation capacity.

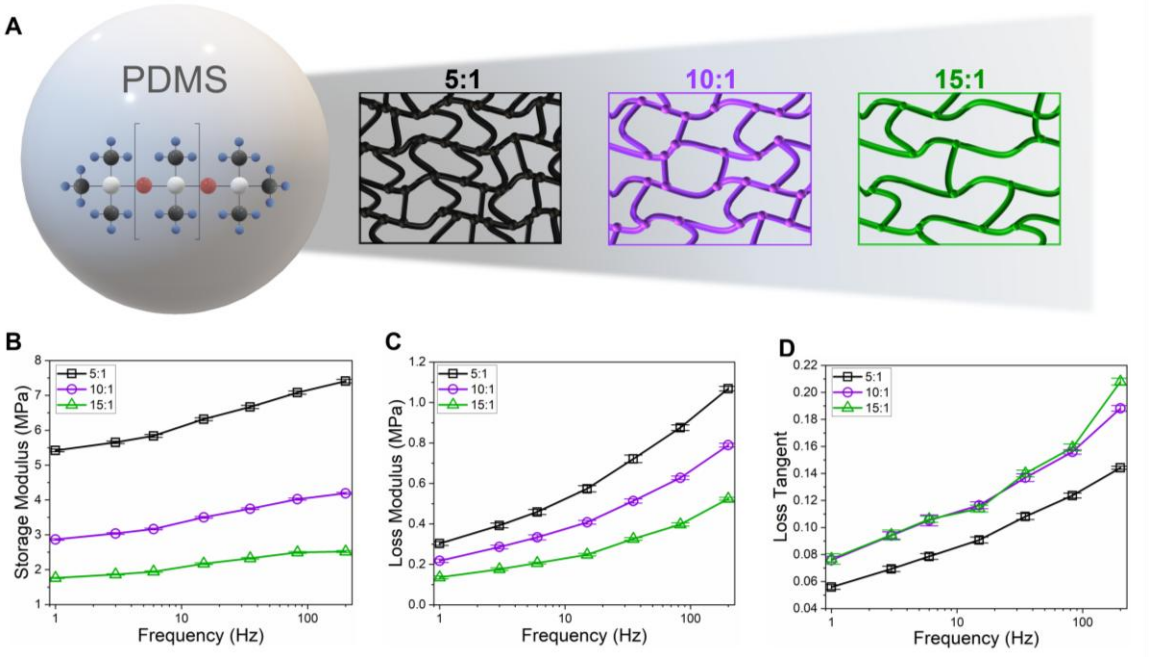

Fig. 1 PDMS composition and viscoelastic response under dynamic mechanical loading. (A) Schematic illustration of PDMS molecular networks with varying crosslinking degrees for 3 different compositions. Comparison of (B) storage modulus (E'), (C) loss modulus (E''), and (D) loss tangent (tan δ) of various PDMS composition samples tested under the probe DMA mode under a flat-punch nanoindenter at frequencies between 1 and 200 Hz. Data points represent mean values from 16 measurements collected over 4 independently prepared samples; error bars indicate the standard deviation.

Further, the surface adhesion of the sample films was examined using both - a macroscopic test and a microscale measurement by nanoindentation. The adhesion values on the macroscopic scale were extracted using the INSTRON testing system by measuring the overall separation force (N) across the entire 2.5 x 2.5 cm^2 sample interface (Table 1). As expected, the higher adhesion was measured for the formulations with the higher ratio between the base polymer and a CA. This is attributed to the enhanced viscoelasticity, lower storage modulus, and greater stress relaxation ability of PDMS with lower cross-linking density. This combination of mechanical properties enables the material to deform more easily, conform more effectively to surface irregularities, and maintain contact during detachment[27-29].

Table 1. Comparison of cross-linking density, molecular weight between cross-links pull-off force, pull-off stress, work of adhesion and separation force of different PDMS compositions.

PDMS composition	Cross-linking density (m^{-3})	Molecular weight between	Pull-off force (mN)	Pull-off stress (mPa)	Work of adhesion (pJ)	Separation force (N)

		cross-links (g mol^{-1})				
5:1	$8.76\times10^{26}\pm4.90^{25}$	1416±79	0.173 ± 0.002	0.082 ± 0.001	196 ± 2	11.15± 1.19
10:1	$4.64\times10^{26}\pm3.51^{25}$	2676±203	0.181 ± 0.003	0.085 ± 0.001	273 ± 5	12.30± 1.90
15:1	$2.85\times10^{26}\pm2.19^{25}$	4350±334	0.164 ± 0.001	0.077 ± 0.001	304 ± 3	13.75± 2.42

The nanoindentation method provides localized measurements at the microscale. By combining macroscale and microscale techniques, it is possible to assess the overall and local adhesion characteristics of the samples. For the 5:1 and 10:1 samples a consistent trend is observed: as the material becomes less cross-linked, all parameters – pull-off force, pull-off stress, and work of adhesion – increase (Table 1). Interestingly, the least cross-linked sample 15:1 deviated from this trend. While it exhibited the highest work of adhesion, both the pull-off force and pull-off stress were lower compared to other compositions. This divergence may be attributed to excessive material deformation, which can reduce effective stress transfer during detachment despite stronger energy dissipation at the interface[29-31]. These results highlight that beyond a certain level of softness, the mechanical response of the material may limit the measurable adhesion forces, even when interfacial bonding is more prominent.

The load-depth curves obtained from nanoindentation (Figure 2 (A)) further illustrate the distinct adhesion characteristics of the three sample compositions. A representative example of a load–depth (P–h) curve during a pull-off test is shown in Figure 2 (B), where δ_{contact} is the indentation depth at the jump-to-contact point, $\delta_{\text{pull-off}}$ and $F_{\text{pull-off}}$ are the indentation depth and the load at the point of maximum adhesive force, respectively. W_{adhesion} is the work of adhesion incurred during one loading cycle, quantifiable by integrating the shaded area under the $P-h$ curve. For the 5:1 and 10:1 samples, decreasing in cross-linking degree results in curves that are both slightly wider and exhibit higher pull-off force, corresponding to greater resistance during probe detachment and higher work of adhesion. Additionally, the slope of the loading and unloading segments is steeper for the 5:1 composition, reflecting its higher stiffness, which is consistent with the probe DMA results discussed earlier. In contrast, the 15:1 composition displays notably different curve profile – shallower in load (lower $F_{\text{pull-off}}$) but significantly broader in depth – indicating that the material undergoes greater viscoelastic deformation and slower recovery during the unloading stage. Despite the lower pull-off force and stress, the increased change of depth during unloading leads to a larger integrated area under the load-depth curve, which translates to a higher calculated work of adhesion (Table 1). This behaviour underscores the role of viscoelastic energy dissipation in soft materials and rubbery polymers (elastomers), where substantial deformation can dominate the adhesion response even when the maximum applied load is reduced[32-34].

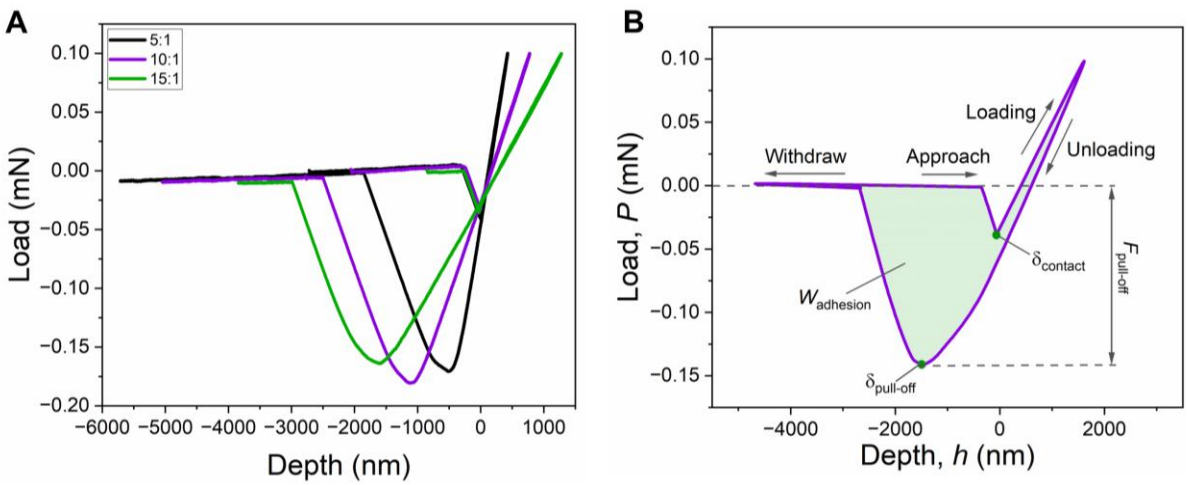

Fig. 2 Nanoindentation pull-off response of PDMS. A) Load-depth curves of 3 PDMS compositions during a pull-off test performed by nanoindentation. (B) Schematic illustration of a typical nanoindentation load–displacement curve.

Surface chemical properties play a critical role in determining the charge affinity of polymers, which directly impacts their performance in triboelectric generators[35,36]. Attenuated total reflectance Fourier transform infrared spectroscopy (ATR-FTIR), Nano-FTIR, X-ray photoelectron spectroscopy (XPS) and Raman spectroscopy were employed to detect changes in chemical bonding and molecular structure associated with varying crosslinking levels. These vibrational spectroscopy techniques are suited for identifying functional group modifications and evaluating differences in surface and bulk chemical environments, which may influence charge transfer behaviour and interfacial interactions[37]. Infrared spectroscopy was used to assess the chemical structure of the three PDMS compositions (Figure 3 (A)). All samples exhibited characteristic peaks associated with PDMS, confirming their consistent base chemistry. Typical absorption bands include Si-CH_3 symmetric and asymmetric deformation modes near 1260 cm^{-1} and 800 cm^{-1} and the Si-O-Si stretching vibration around 1000 – 1130 cm^{-1} [38]. Notably, subtle but consistent differences were observed between the samples. In the Si-O-Si stretching region (~1060 cm^{-1}), which typically presents as a double peak[39], a variation in intensity was evident in the lower part of this feature: the 5:1 composition with the highest cross-linking agent concentration showed the lowest intensity, followed by the 10:1 composition, while the 15:1 composition with the lowest cross-linking agent concentration exhibited the highest intensity of absorbance peak. This trend may reflect differences in siloxane network flexibility or crosslinking density, which influence segmental mobility. The variation in the Si-O-Si stretching intensity is a direct reflection of the cross-linking density and flexibility of the siloxane network. Higher cross-linking agent concentration results in a more rigid network with lower vibrational intensity, while lower concentrations allow for greater flexibility and higher intensity[40,41].

Changes in the intensity of the peak at 910 cm^{-1} are attributed to Si-H asymmetric bending[42]. CA of Sylgard 184 is known to possess both Si-H and Si-CH_3 groups along its backbone[43]. From the results, we see that the highest intensity is for 5:1 composition, where CA content is around 17 wt%, while it decreases both for 10:1 composition (CA ≈9 wt%) and 15:1 composition (CA ≈6 wt%) for which the peak is almost indistinguishable. The presence of Si–H bonds in the CA promotes cross-linking between siloxane backbones containing vinyl groups (Si-C_2H_3) via the hydrosilylation reaction[44]. Results indicate that for the 5:1 composition, there is a larger fraction of unreacted Si-H bonds than in 10:1 or 15:1 compositions, which is in line with results reported in other studies[44].

These findings are further supported by nano-FTIR measurements (Figure 3 (B)), which probe the near-surface region and reveal no significant changes in characteristic Si–O–Si and –CH_3 vibrational modes across different compositions, confirming that the surface chemical structure remains largely unchanged. Representative nano-FTIR spectra acquired at multiple surface locations, together with the corresponding near-field IR absorption maps and AFM topography images, are provided in Supplementary Information (Figures S1–S3).

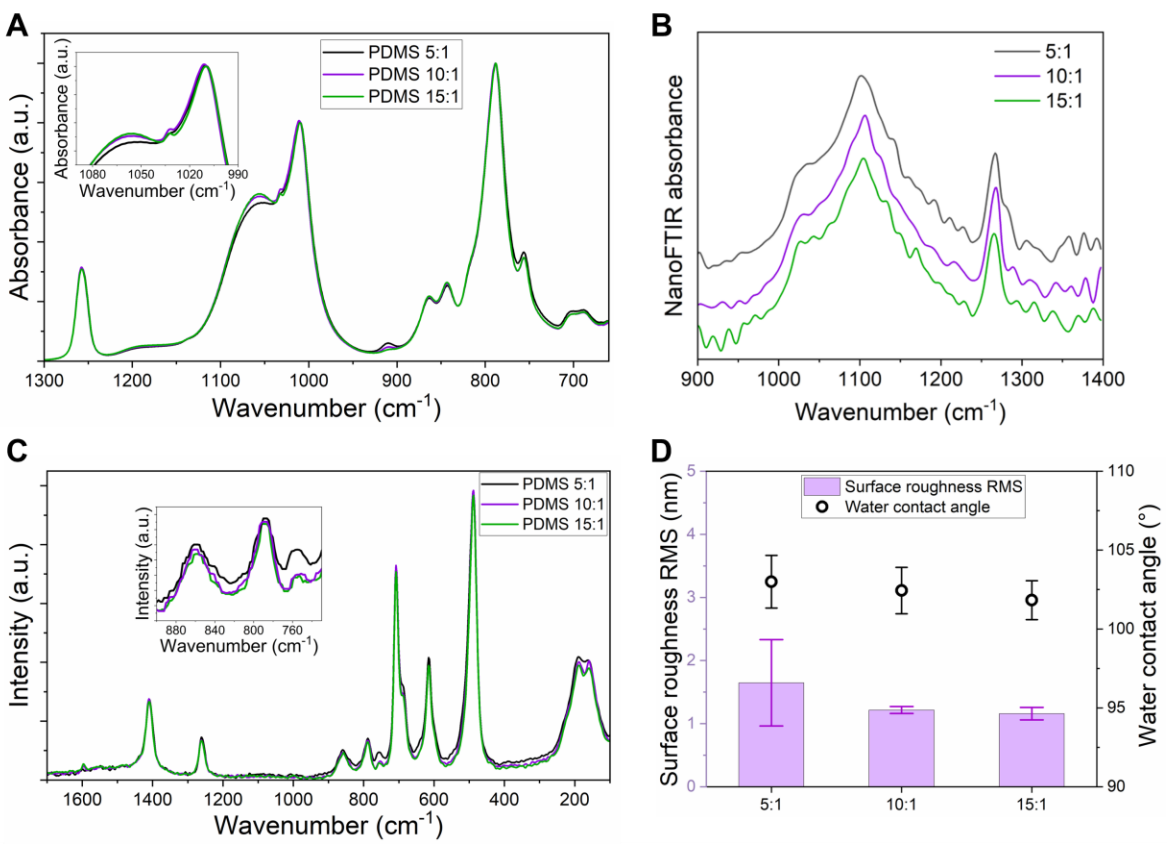

Fig. 3 Spectroscopic characterization of PDMS. ATR-FTIR (A), NanoFTIR (B) and Raman (C) spectra of different PDMS compositions. (D) Surface roughness and water contact angle of different PDMS compositions.

Raman spectra also displayed the typical peaks associated with PDMS (Figure 3 (C)). Key Raman-active modes include strong Si-O-Si symmetric stretching near 490 cm^{-1}, Si-C stretching around 710 cm^{-1} and characteristic band near 1410 cm^{-1} corresponding to CH_3 deformation[45]. A subtle difference was observed at approximately 760 cm^{-1}, a region often attributed to Si-CH_3 rocking or bending vibrations[46]. The 5:1 composition showed the most intense peak at his position, while the 10:1 and 15:1 samples exhibited slightly lower intensities. This trend may reflect differences in chain packing or crosslinking density, where a stiffer network structure in the 5:1 sample enhances Raman activity in this mode[24,47]. These Raman findings align with FTIR observations.

These spectroscopic distinctions, though subtle, provide further evidence of underlying structural differences across the compositions that likely contribute to their differing macroscopic behavior. The CA contains both -H and -CH_3 functional groups on Si-O-Si backbone[43]. The hydride groups participate in hydrosilylation with the –CH=CH_2 groups of the base prepolymer, forming Si–CH_2–CH_2–Si crosslink sites (supplementary information, scheme S1). However, the changes in the ratio between C-C bonds and Si-O bonds are small as evident from differences in the peak intensities (<4%) and shouldn't create an impact on the chemical structure (i.e. charge affinity) of the surface.

Surface-sensitive XPS measurements were performed to examine whether the PDMS base to CA ratio influences the near-surface chemical composition. Two independently prepared samples were analysed for each composition (5:1, 10:1, and 15:1). As shown in Supplementary Information Fig. S4–S6, the Si 2p, C 1s, and O 1s spectra appear similar across all compositions in terms of overall peak shape and component structure. Within the limits of the fitting procedure, the Si 2p spectra can be described by contributions tentatively assigned to Si–C, Si–O–Si, and more oxidized Si species, while the C 1s spectra are dominated by components consistent with C–Si and C-C/C–H bonds characteristic of PDMS methyl groups and crosslinks. The O 1s spectra likewise show features attributable to Si–O–Si bonding. No clear or systematic shifts in binding energy or consistent changes in relative peak intensities were identified as a function of base to CA ratio. Any observed variations fall within the instrumental energy resolution of the XPS system (0.1 eV) and the uncertainty associated with peak fitting. Measurements from independently prepared samples show comparable spectral features, suggesting reasonable reproducibility, although minor differences cannot be fully excluded given the fitting uncertainty.

Surface roughness and wettability were also evaluated (Figure 3 (D)). All PDMS samples exhibited similarly low root mean square (RMS) roughness values – 1.65 ± 0.68 nm (PDMS 5:1), 1.22 ± 0.06 nm (PDMS 10:1), and 1.16 ± 0.10 nm (PDMS 15:1) – which are comparable to the ITO substrate (2.05 ± 0.11 nm). In addition, water contact angle measurements showed minimal variation across compositions (102.99 ± 1.67°, 102.44 ± 1.47°, and 101.83 ± 1.23° for PDMS 5:1, 10:1, and 15:1, respectively), indicating similar surface wettability. These results suggest that the PDMS surfaces are chemically and morphologically comparable across different base to crosslinker ratios.

The effect of adhesion on triboelectric charge

The three different compositions of PDMS were tested to study the influence of surface adhesion on triboelectric charge, by contacting them against ITO in single electrode mode as showed in Figure 4 (A). The experimental results are presented in Figure 4 (B) and (C). PDMS samples exhibiting stronger adhesion to ITO also demonstrate larger charge density. The measured separation force curves are presented in supplementary figure S7. With increase in the average separation force from 11.15 ± 0.22 N to 13.75 ± 0.20 N the charge density increases and becomes more negative from –0.18 ± 0.01 nC cm^{-2} to –0.47±0.01 nC cm^{-2}. This can be attributed to charge (organoion) transfer due to covalent bond breakage, as the softness and adhesion increases[8,48]. In PDMS, covalent bond scission can occur at Si–C crosslinks formed by the curing agent, producing positively charged fragments that can transfer to the counter surface, while the Si-terminated PDMS surface becomes negatively charged[49,50]. Under strain or due to adhesion, backbone Si–O–Si bonds may also rupture, generating oxygen-rich negatively charged fragments and complementary positively charged silicon fragments[6,51]. Once generated, these fragments can remain on the counter surface, recombine or reattach to PDMS, or redistribute in subsequent contact–separation cycles, allowing triboelectric charge generation to persist over multiple cycles. Prior studies have linked organoions as the charge species in contact electrification[52,53], proven via XPS, AFM[11,54], Raman[55] and IR spectroscopy[56]. Furthermore, a clear correlation between adhesion force and surface charge has been observed[8]. In highly adhesive interfaces, the energy of the formed adhesive (physical) bonds between contacting surfaces may exceed the energy of chemical or physical bonds within the bulk[57]. The increase of adhesion forces enhances the likelihood of covalent bond scission and organoion transfer, contributing to the observed triboelectric effects[8]. On the other hand, softer materials undergo a larger extent of deformation, thus increasing the specific contacting area and enhancing charge transfer[58].

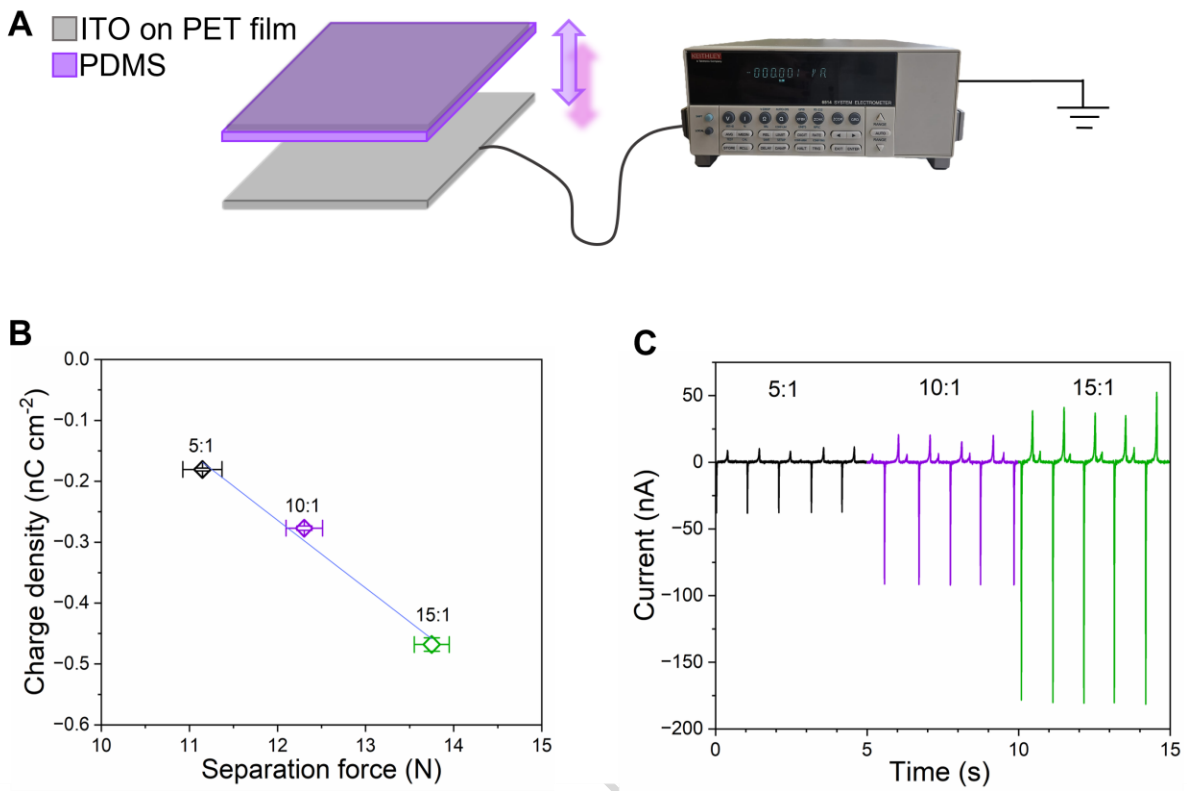

Fig. 4 Adhesion-dependent triboelectric response of PDMS. (A) Schematic of single electrode measurement setup. Separation force and charge density correlation (B) and current peaks (C) of various PDMS compositions, tested against ITO in single electrode mode. Error bars in (B) represent the standard deviation calculated from three independently prepared PDMS samples.

To evaluate whether the observed increase in triboelectric charge density could originate solely from variations in real contact area under identical nominal loading (10 N), we performed a contact mechanics analysis. The predicted real contact area between the 5:1 and 15:1 compositions increases by a factor of 2.11. This larger contact area allows the formation of more adhesive bonds at the interface, which can rupture during separation, facilitating greater organion transfer. The experimentally measured charge density increases by a factor of 2.61, indicating that the enhancement arises from the coupled effect of increased real contact area and interfacial adhesion rather than from contact area alone. AFM measurements show comparable RMS roughness values for all PDMS compositions (≈1.5 nm), which are similar to the roughness of the ITO counter surface (2.05 ± 0.11nm), indicating that surface topography remains effectively unchanged across samples. Water contact angles are also nearly identical (≈102°) (Fig. 3 (D)), confirming consistent surface chemistry.

Classical molecular dynamics (MD) simulations further demonstrate an increase in polymer flexibility while the ratio base to CA decreases. To provide a qualitative description of this behaviour, structural features such as the radius of gyration (R_g) and the solvent accessible Fsurface area (*SASA*) were analyzed (Table 2 and Fig. S8; see the *Computational Methods* section for more details).

R_g, defined as the average distance of atoms from the center of mass of the system, increases as the degree of cross-linking decreases. However, this trend is partially influenced by the different sizes of the simulated systems: the 5:1 model contains fewer atoms, whereas the 10:1 and 15:1 systems are comparable in size. Notably, the 15:1 system exhibits significantly larger fluctuations in R_g compared to the other models, indicating enhanced conformational flexibility.

Table 2. Gyration radius (R_g), solvent accessible surface area (*SASA*) and roughness ratio calculated from classical molecular dynamics simulations for the three cross-linked polymer systems.

PDMS composition	R_g (Å)	SASA (Å^2)	Roughness ratio
5:1	8.85 (0.10)	1334.5 (57.3)	1.6
10:1	10.13 (0.07)	1465.7 (57.3)	1.8
15:1	9.97 (0.15)	1423.7 (109.9)	1.8

To reduce the influence of system size, SASA was evaluated by considering only the surface exposed to vacuum. In contrast to R_g, the average SASA values are more similar across the three systems, although the overall trend is preserved. The 5:1 system exhibits the lowest SASA, which increases for the 10:1 system and slightly decreases for the 15:1 system. Importantly, the 15:1 model shows the largest standard deviation, whereas the 5:1 and 10:1 systems display comparable fluctuations. This behavior suggests that the 15:1 polymer has higher mobility and can more readily access configurations with increased exposed surface area. These qualitative findings are consistent with experimental observations indicating that a lower degree of cross-linking enhances polymer deformability and that, as a result, the cross-polymer can undergo greater deformation under load. The surface roughness was further quantified through the roughness ratio, defined as $SASA/(2A_{xy})$, where A_{xy} is the projected area of the simulation box in the x-y plane. This dimensionless parameter equals 1 for an ideal flat surface and increases with surface corrugation. Since all simulations were performed at constant volume, A_{xy} remains constant across systems. Accordingly, the 5:1 system displays the lowest roughness, while the 10:1 and 15:1 systems exhibit comparable average roughness values.

Together, the aforementioned results indicate that although variations in real contact area contribute to the triboelectric response, the observed increase in charge density with decreasing

crosslinking ratio exceeds contact-area scaling and is therefore attributed to enhanced adhesion accompanied by improved interfacial conformity and chain mobility at lower crosslinking densities.

Interestingly, for all compositions, the first separation cycle exhibited a noticeably lower force peak compared to subsequent cycles. As the number of cycles increased, the separation force increased and reached a steady-state value by approximately the 10th cycle as shown in supplementary figure S9 (A-C). The relative increase in separation force between the first and the tenth cycle was 14%, 9% and 19% for the 5:1, 10:1 and 15:1 compositions, respectively. This can be attributed to electrostatic attraction from triboelectric charges[59] or due to formation of free polymer chains from bond rupture that may entangle with the molecules on the opposite film, thus providing stronger adhesion[14]. Control experiments were performed using ion-assisted charge neutralization. For each PDMS composition, contact–separation measurements were conducted, recording the stable separation peak (10th contact separation cycle) and the first peak after 1 min of ion flow from ion-blower. As shown in Fig. S9 (D), charge neutralization did not affect the magnitude of the adhesion peak or the composition-dependent trend (15:1 > 10:1 > 5:1). The comparable adhesion forces before and after ion neutralization indicate that electrostatic interactions do not significantly contribute to the measured separation force. Instead, the adhesion is dominated by intrinsic interfacial interactions, such as polymer chain stretching and rupture during separation.

When tested against ITO, all three PDMS compositions exhibited the same negative charge polarity. This coincides with the tendency of PDMS to occupy a negative position in the triboelectric series when paired with hard, smooth conductive oxides such as ITO[51,60,61]. In this case, the nature of the counter surface appears to dominate the polarity outcome, while the differences in base and CA ratio primarily influence the magnitude of the generated charge. The observed correlation between adhesion and triboelectric charge density highlights adhesion engineering as a practical strategy for controlling contact electrification through simple composition adjustments. Unlike conventional approaches that require changing material pairs or introducing additional surface modifications, tuning adhesion via curing composition preserves material chemistry while enabling continuous control of charge magnitude. This approach allows mechanical compliance and electrical output to be optimized simultaneously, addressing a common limitation in triboelectric systems where softness, adhesion, and performance are strongly coupled. Such control may simplify device design and enable more recyclable triboelectric generators by avoiding multi-material or coated structures.

To evaluate generality, additional experiments were performed using polyurethane (PU) and Ecoflex 00-30 elastomers with mixing ratios of 1:1, 1:2, and 2:1 (supplementary figure S10). In both systems, higher separation forces against ITO produced higher charge densities while the charge polarity remained consistent with the triboelectric series (PU positive, Ecoflex negative), indicating that adhesion-mediated tuning is not limited to PDMS but may represent a general

mechanism for cross-linked elastomers. Adhesion may also be adjusted using plasma treatment[62,63], additives[64], or localized cross-linking[65], providing multiple routes for controlling triboelectric charge generation.

To reveal the effect of adhesion on charging tendencies, we tested PDMS vs. PDMS samples with the same or different CA ratio (Figure 5). The measurements were performed in a vertical contact-separation mode with two electrodes (Figure 5 (A)). Contacting PDMS films with similar surface adhesion produced a negligible charge of 0.002 nC cm^{-2}. This behaviour can be attributed to the negligible net charge transfer due to the absence of a driving force or to a balanced exchange of the same amount of opposite charges, resulting in zero net charge. Material transfer between polymer surfaces during contact-separation is known to occur in a bi-directional manner[66]. If the mechanical hardness, morphology, and adhesion are the same for both contacted polymer films, the same amount of charges will be exchanged. Bi-directional material transfer may lead to spatially heterogeneous surface charge distributions, often referred to as surface charge mosaics, in which micron-scale regions of positive and negative charge coexist on the same polymer surface[67]. The presence of heterogeneous surface charge distributions does not necessarily imply the simultaneous transfer of both positive and negative charge carriers. Even if charge transfer is dominated by a single carrier polarity, spatially non-uniform contact, electrostatic induction, or partial back-transfer during contact-separation can produce locally varying charge densities, which may appear as charge mosaics[68,69]. It is important to note that charge mosaics may not be ubiquitous and may arise only under specific conditions, such as dielectric breakdown[69]. At the macroscopic level, the observed near-zero net surface charge density may also arise from two effects. First, spatial variations on local contact-separation can produce non-uniform charge distributions whose contributions average to nearly zero, even when charge transfer is dominated by a single polarity. Second, electrostatic induction during contact-separation can drive partial back-transfer or recombination of charges, thereby reducing the measurable net charge[70-72].

When two PDMS films with different adhesion were contacted, the surface charge increased by an order of magnitude. The surface charge 0.06 nC cm^{-2} was measured by contacting PDMS 5:1 vs. PDMS 15:1, which is 6 times higher result than the combination of 5:1 vs. 10:1 and 30 times higher if compared to combination made out of the same composition PDMS (Figure 5(D)). These results highlight the critical role of surface adhesion in triboelectric charge generation.

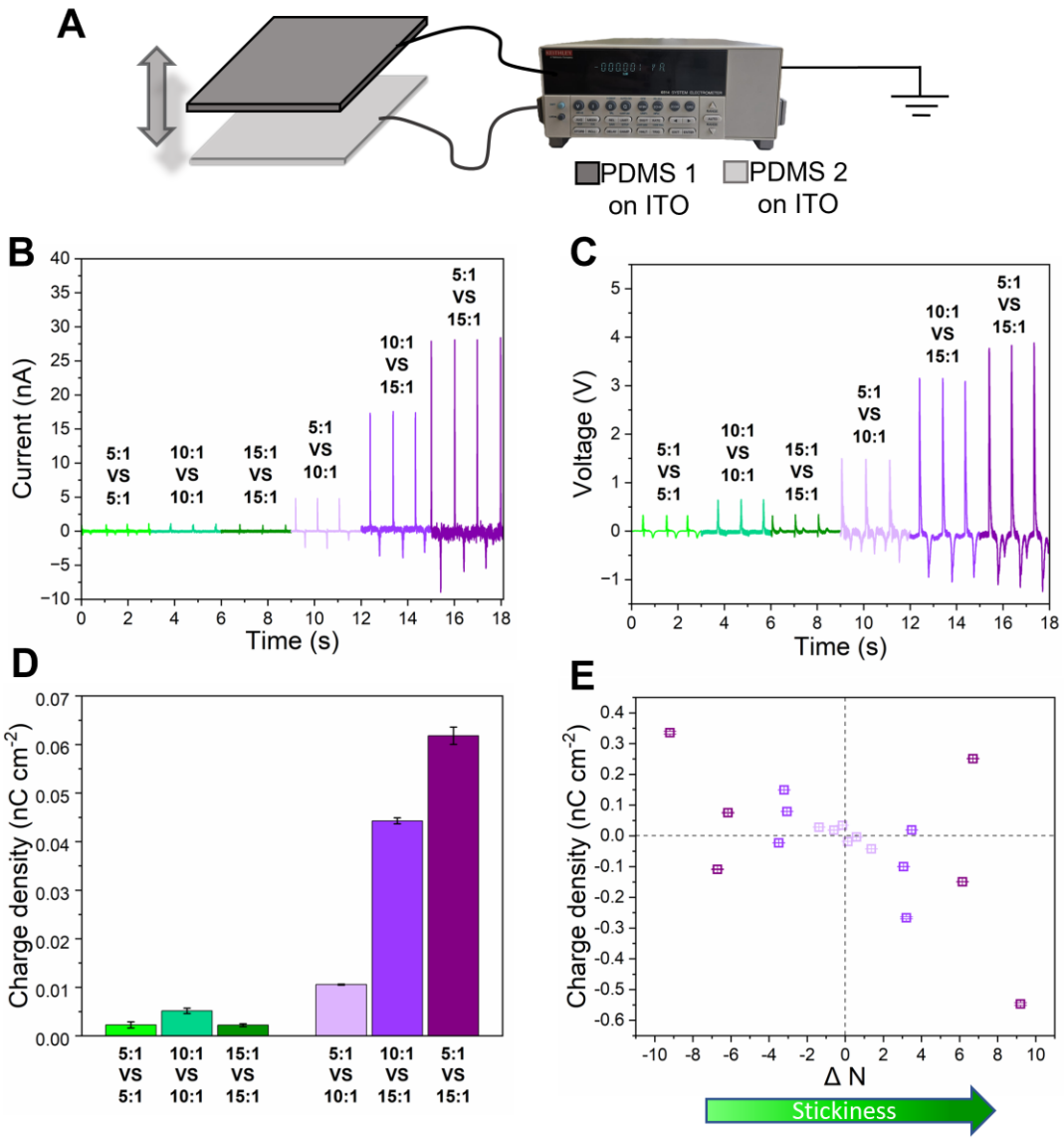

Fig. 5 Triboelectric performance and adhesion-dependent charging in PDMS. (A) Schematic of vertical contact-separation mode measurement setup. Current (B) and voltage (C) peaks. Charge density (D) measured for various PDMS combinations in vertical contact-separation mode, where data points show mean values from three parallel samples (20 peaks per sample; standard deviation). (E) Dependence of charge density on the adhesion difference between different PDMS; each data point corresponds to an individual PDMS–PDMS sample pair averaged over 20 peaks (standard deviation), corresponding the same colour scheme as in (D).

Prior studies have shown that this process is strongly influenced by mechanical softness. It has been reported[11,54] that soft polymers tend to undergo greater mass transfer during contact, with transfer occurring in both directions but predominantly from the softer material to the harder one. Additionally, our group has previously shown[7] that when different polymers are contacted, softer material typically becomes negatively charged while the harder material charges positively. Regarding PDMS polarity, Pandey et al[11] showed that when PDMS films with different stiffnesses (*E*) are contacted against much more rigid PVC, the less crosslinked (lower *E*) PDMS charges more negatively than the more crosslinked formulation (higher *E*). Our results therefore extend existing theory by demonstrating that, even in chemically identical elastomers, adhesion-mediated differences in mechanical response are sufficient to strongly enhance triboelectric charge generation.

Beyond the substantial increase in charge magnitude, we observe that the stickier surface of two PDMS mutually contacted surfaces charges negatively, while the surface with lower adhesiveness charges positively (Figure 5 (E)). Data points for this graph are shown in Supplementary information Table S1. This behaviour is consistent with the fact that more adhesive surface is the one with lower crosslink density and lower *E*, thus providing increased chain mobility and greater conformity to the asperities of the contacted surface. These findings demonstrate that the polarity of triboelectric charge can be modulated through adhesion-mediated mechanical differences between chemically identical elastomers, without substantially altering their surface chemistry. Since bond scission is expected in the material with least crosslinks (lower *E*), mass transfer most likely occurs from the most adhesive PDMS surface to the least adhesive PDMS. Given that most elastomers tend to charge negatively[73-75], enhancing adhesion offers a practical route to boost charge density and tailor polarity in device design simultaneously, especially in configurations where the same material is used for both triboelectric layers.

Electron transfer based on differences in surface electronic structure is one of the mechanisms often proposed to explain charge generation in triboelectric systems. To examine whether variations in the base agent to curing agent ratio could introduce electronic differences that influence charge transfer, we calculated the surface work functions of the three PDMS formulations using density functional theory (DFT) calculations implemented in Vienna Ab initio Simulation Package (VASP). More details on DFT calculations and how to compute work function are described in the Computational methods. The resulting work functions are very similar, with values of 5.78 eV for 5:1 PDMS, 5.91 eV for 10:1, and 5.89 eV for 15:1. From a qualitative standpoint, all three polymers exhibit work function values higher than that of ITO (4.62 eV), as calculated using the same methodology reported in the literature[76]. This indicates that electron transfer from ITO to the polymers is energetically favoured, leading to the accumulation of negative charge density on the polymer surfaces, in agreement with experimental observations. However, the values above lie within a narrow range, with a maximum difference of only ~0.1 eV, indicating that the intrinsic electronic properties of the three formulations are nearly identical. Such a small variation cannot account for the substantial differences in triboelectric charge magnitude

and polarity observed experimentally. This suggests that variations in electron affinity associated with the base agent to curing agent ratio are unlikely to be the dominant driving force for charge transfer between the PDMS surfaces. Instead, the experimental trends are more consistent with adhesion-mediated effects arising from differences in crosslink density, which influence surface mobility and the extent of interfacial mass or organoion transfer during contact-separation.

Influence of compression time to change the interfacial adhesion

To further investigate the role of contact conditions, we conducted additional measurements in the Instron tester focusing on the effect of contacting time on both charge generation and interfacial adhesion. PDMS film samples were tested against ITO electrode in the single electrode measurement setup as shown before in Figure 4 (A). The results reveal that both charge density and separation force are strongly dependent on the compression time (Figure 6 (A)).

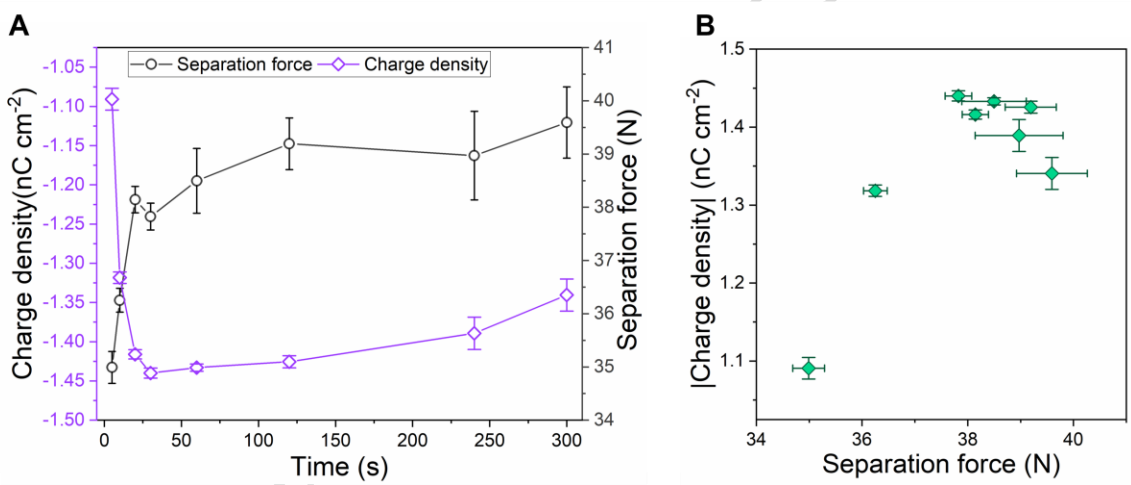

Fig. 6 Charge-force relationships in PDMS triboelectric testing. Charge density and separation force dependence on compression time (A) for PDMS, tested against ITO in Faraday cup mode. Charge density dependence on separation force (B) for PDMS. For each compression time, measurements were performed on an independently prepared PDMS sample; data points represent mean values calculated from five current and force peaks, and error bars indicate the standard deviation.

Separation force initially increases with compression time, indicating that a more prolonged contact enhances interfacial interactions, possibly due to the formation of more adhesive intermolecular bonds, molecular rearrangement, or improved contact conformity as a function of time[77,78]. However, beyond 60 seconds, the separation force reaches a plateau within experimental uncertainty, suggesting that a maximum effective contact and adhesion has been achieved. Some decrease may be due to viscoelastic relaxation[79,80]. A similar non-monotonic trend is seen in charge density, which sharply increases and then slightly decreases. Such behaviour has been reported for several polymer systems and is generally attributed to competing processes, including charge accumulation, redistribution, and dissipation at extended compression times[81]. Importantly, this

decrease does not indicate material degradation but rather reflects interfacial dynamics under prolonged static contact. Cyclic contact-separation measurements over 5,000 cycles (Supplementary Fig. S11) shows stable output after an initial increase (~1,000 cycles), indicating that the observed decrease at extended contact times does not compromise long-term device performance.

Notably, a correlation is observed between separation force and absolute values of charge density (Figure 6 (B)), indicating that increased adhesion between PDMS and ITO leads to higher charge generation. While contact time dependent changes in triboelectric output have been reported, they are typically not directly linked to adhesion[81,82]. The present results therefore provide direct evidence that interfacial adhesion plays a key role in charge generation, highlighting the importance of adhesion-mediated interfacial interactions.

Conclusion

In this work, the mechanical properties and surface adhesion of PDMS was effectively varied by changing the degree of crosslinking. The least crosslinked PDMS shown pronounced mechanical softness, as well as highest separation force and work of adhesion. Moreover, the less cross-linked PDMS also shown tendency to exhibit a larger surface charge density upon contact-separation versus ITO due to enhanced specific contacting area and organoion transfer. Upon identical PDMS vs PDMS material contact the more adhesive (less cross-linked) surface acquired negative surface charge, while the less adhesive PDMS became positively charged. This work demonstrates the significance of surface adhesion on triboelectric charge density and polarity. This new knowledge can be used to tune the triboelectric charging of materials in future.

Methods

Sample preparation

PDMS (DOW, Sylgard^{TM} 184) samples were made by mixing base polymer and CA in different weight ratios (5:1; 10:1, and 15:1) and spin-coated on the indium tin oxide (ITO) substrate at 2500 rpm for 10 s. Polyurethane (Alchemie, PU 3544) and Ecoflex 00-30 (Smooth-On, Ecoflex^{TM} 00-30) were made by mixing components A and B in different weight ratios (1:1, 1:2, 2:1) and spin-coated on the ITO substrate at 2500 rpm for 10 s. Then, all samples were cured at 80 °C for 24 h. The size of the obtained sample films was 5 cm^2 and the thickness was 100 µm.

Material characterization

ATR-FTIR measurements were performed to determine structural differences of various compositions of PDMS by using Nicolet iS10 FTIR spectrometer equipped with an attenuated total reflectance (ATR) module.

The atomic force microscopic (AFM) height topography and nano-FTIR spectral measurements of the PDMS membranes were carried out using a scattering-type scanning near-field optical microscope (Neaspec s-SNOM), with a 20 nm spatial resolution.

The chemical composition was studied using Raman spectroscopy which was performed with Renishaw InVia Reflex confocal Raman microscope. Raman spectra were collected in the range of 300 to 1700 cm^{-1} under irradiation with 514 nm laser using 20 mW laser power.

XPS measurements were performed using ThermoFisher ESCALAB Ti+ (Brno, Czechia). Six (two for each composition) PDMS samples for the measurement were prepared on a conductive ITO/glass substrate. The PDMS did not cover the entire conductive area; an uncovered region was intentionally left to attach a grounding contact, and the contact was connected during measurement. Charge neutralisation was enabled using the flood gun at an emission current of 20 µA. Spectra were acquired using the monochromated Al Kα source (mono anode XR6 gun) with a 650 µm spot. Automated height adjustment was enabled around the initial focus point over ±500 µm in 50 µm steps. High-resolution core-level regions were acquired in constant analyser energy mode at 10 eV pass energy with 0.1 eV steps using 10 scans and 75 ms dwell per point for Si 2p (95–110 eV), O 1s (525–545 eV), and C 1s (279–298 eV). The data was processed using Thermo Avantage v5.993.

Surface roughness was determined from atomic force microscopy (AFM) topography measurements performed by Veeco CPII scanning probe microscope. Measurements were done using PtIr probe. Surface roughness was calculated as the average of measurements at two different locations on the sample with a 20 × 20 µm scan area for two parallel samples for each composition. The error corresponds to the standard deviation from 4 measurements.

The contact angle was determined using a drop shape analyzer (DSA25, Kruss) by using the Young Laplace model for contact angle determination. Sample liquid was deionized water, and the measurement temperature was 20 °C. For each PDMS composition, three independent samples were analyzed, with four droplets measured per sample. The reported contact angle values therefore represent the average of 12 measurements, and the associated error corresponds to the standard deviation.

To study the mechanical properties, probe-based dynamic mechanical analysis (probeDMA) was performed implementing the technique developed for the KLA iMicro nanoindenter. A flat-ended diamond cylindrical punch (radius = 26 µm) was used to apply an oscillating stress on the sample at varying frequency, and the resultant displacement oscillation was recorded to reveal information about the storage modulus, loss modulus and the loss tangent of the viscoelastic sample. The storage modulus (E') is a measure of stored energy under deformation and quantifies the elastic property of the sample. The loss modulus (E'') quantifies the viscous response, and it measures energy dissipation during loading cycle. The ratio of loss modulus and storage modulus gives the loss tangent ($\tan\delta = E''/E'$), which characterizes damping in the material by energy dissipation. Measurements were performed on four independently prepared PDMS films for each base to

curing agent ratio. A total of 16 tests were performed in 4 discrete regions on a 2.5 × 2.5 cm^2 nominal sample area, and 4 points were selected in each region. Using the obtained storage moduli values at 1 Hz, the molecular weight between crosslinks (M_C) was calculated with the formula

$$M_C = 3\rho R_g T E^{-1} \quad (1)$$

where ρ is the density of polymer, R_g the gas constant and T the absolute temperature[83]. Crosslink densities were calculated using formula

$$E = \frac{3}{2} kT\rho_K \quad (2)$$

where E is tensile modulus, k is the Boltzmann constant, and T is the absolute temperature[84]. For calculation of both these parameters, E and T values were taken from probeDMA measurements for each PDMS composition at 1Hz. The polymer density (ρ) was assumed to be 1.03 g cm^{-3}, as previously determined by hydrostatic weighing for the 10:1 composition[15]. Reported densities for the 5:1 and 15:1 compositions in the literature fall within the experimental error limits of this value[85]; hence, a density of 1.03 g cm^{-3} was applied to all samples. Absolute errors for crosslink density and molecular weight were calculated by uncertainty propagation based on partial differentiation of the corresponding equations with respect to the storage modulus (E) and temperature (T). As the loss tangent at 1 Hz frequency is low (under 0.08), indicating that the material response was elastic, we can assume that storage modulus E' is a good approximation of tensile Young's modulus E for the purpose of calculating crosslink density[86].

During the pull-off test performed in the iMicro nanoindenter, a cylindrical flat punch with a radius of 26 µm was initially withdrawn 2 µm from the sample surface, ensuring that the tip was fully out of the adhesion interaction zone. The tip then started approaching the surface at a speed of 100 nm s^{-1} until it was in the vicinity of the surface. To allow more accurate surface detection, the phase signal was monitored in this process until a phase change larger than 15° was detected. After contacting the surface, an indent was performed at a loading rate of 0.01 mN s^{-1} to a maximum load of 0.1 mN. The tip was held in peak load position for 2 s before it was unloaded at the same rate, and eventually withdrawn 5 µm from the sample surface. The nominal pull-off stress was determined by dividing the pull-off force by the contact area of the flat-ended punch (nominal area = 2124 μm^2). Pull-off force and pull-off stress values were averaged from 12 measurements performed on different regions of the same sample. The work of adhesion was determined by calculating the enclosed area established under the load-depth curve. Measurements were performed on three independently prepared PDMS films for each base-to-curing-agent ratio. A total of 12 tests were performed in 3 discrete regions on a 2.5 × 2.5 cm^2 sample area and 4 points were selected in each region. Work of adhesion values were calculated by integrating the area under the load-depth curve and averaged from 12 separate measurements.

To evaluate the influence of mechanical properties on real contact area under identical nominal load (10 N), we performed a relative comparison based on the Johnson-Kendall-Roberts (JKR)

contact model[87]. Within this framework, the contact radius depends on the effective elastic modulus, and for materials with identical surface energy and geometry, the real contact area scales with the effective Young's modulus as

$$A \propto (E*)^{-\frac{2}{3}} \quad (3)$$

Using the measured storage modulus values as the effective Young's moduli for each composition, relative changes in contact area between samples were calculated to assess the mechanical contribution to the triboelectric response.

Triboelectric measurements

The contact-separation study was carried out using an Instron E1000 material testing machine, which ensures the repeatability of triboelectric measurements. They were performed under controlled conditions – a separation distance of 5 mm, a compression force of 10 N, and a separation speed of 0.1 m s^{-1}. All experiments were conducted under ambient laboratory conditions at a temperature of 22-23 °C and relative humidity of 30-35%. Before testing all samples (both PDMS and ITO) were cleaned in air plasma for 1 min (Harrick Plasma PDC-002-CE) to remove contamination that could affect the measured charge.

The generated current signals were measured using a Keithley 6514 electrometer connected to a Picoscope 5444B PC oscilloscope system. Surface charges, *Q* (nC), were calculated by

$$Q = \int i \, dt \quad (4)$$

where *i* is the instantaneous current (nA) and d*t* is the differential of time (s). Integration was done for the high, narrow peaks, which correspond to the separation stage. The charge generated by individual PDMS films was determined after contact-separation with ITO, which was connected to an electrometer, and the current was measured against ground. This measurement setup was used as a single-electrode mode to determine the magnitude and polarity of triboelectric charges formed on the PDMS samples, as well as to measure the force (N) necessary for separation of PDMS films. Three parallel sets of sample pairs were tested for each combination. The separation force values were taken from dynamic mechanical tests and averaged from 20 contact-separation peaks of each sample.

When PDMS–PDMS contact–separation experiments were performed in single-electrode mode, one PDMS film coated on the ITO substrate served as the sensing electrode in the same manner as the ITO electrode described above. By alternating which PDMS/ITO electrode was connected to the electrometer, the polarity of triboelectric charge formed on the opposing PDMS surface was identified from the sign of the measured current peaks. The same experiment was repeated with two electrometers to show that simultaneous monitoring of both contacting samples yields

consistent current signals and confirms the polarity assignment obtained with the single-electrometer configuration as shown in Fig. S12. The separation force difference (ΔN) between two PDMS samples was calculated as

$$\Delta N = N_1 - N_2 \quad (5)$$

where N_1 and N_2 are the mean separation forces obtained independently for each PDMS composition against ITO electrode in single electrode mode. For a PDMS-PDMS pair, ΔN therefore depends on the chosen reference sample, and the sign of ΔN reverses when the subtraction order is inverted (e.g., 5:1 against 10:1 versus 10:1 against 5:1). This allowed us to isolate the intrinsic triboelectric properties of each PDMS composition sample before testing them against one another, reducing the effect of adhesion and mass transfer between PDMS surfaces.

The PDMS films were also tested against one another in vertical contact-separation mode. Since the PDMS layers were spin-coated on ITO substrates, the ITO coatings served as the back electrodes, forming a two-electrode configuration. The electrometer was connected to both electrodes, therefore measuring the short-circuit current generated during cyclic contact-separation. The measured current corresponds to charge flow in the external circuit induced by the triboelectric charges formed at the PDMS-PDMS interface.

Computational methods

Description of computational samples. Cross-linked systems were constructed by preserving the key chemical features of the experimental samples while reducing the system size to enable feasible DFT calculations and geometry optimizations within a reasonable computational cost. To this end, a model base polymer consisting of 25 repeating units (shorter than the experimental average length of ~60 units) and terminated with two vinyl groups was employed. The curing agent was modeled at its experimental size (10 repeating units) and included two Si–H functional groups. Different cross-linking ratios were generated as follows. For the 5:1 system, (corresponding to the highest cure agent concentration), two cure agent molecules were fused with a single base polymer, resulting in an excess of Si–H groups. In the 10:1 system, two base polymer chains were cross-linked with two cure agent molecules, leading to complete reaction between vinyl and Si–H groups. For the 15:1 system, corresponding to the lowest cure agent concentration, two base polymer chains were fused with one CA molecule, resulting in an excess of vinyl groups. The final models consist of 481 atoms for the 5:1 system, 760 atoms for the 10:1 system, and 659 atoms for the 15:1 system.

Classical Molecular dynamics simulations. MD simulations were performed using LAMMPS code[88]. Polymeric slabs were constructed by placing the three cross-linked systems in a simulation box with lateral dimensions of 20x20 $Å^2$ along x-y plane and a length of 100 Å along the z direction, in order to minimize spurious interactions. Periodic boundary conditions were applied in all three directions. Interatomic interactions were described using the Dreiding force field[89,90], which has been shown to provide reliable structural predictions for PDMS polymers[91]. Initial

velocities were assigned according to a gaussian distribution corresponding to a temperature of 200 K. The systems were then heated to 300 K *via* an annealing procedure. The pre-production (2 ns long) and production runs (5 ns) were performed within the constant number of particles, volume, and temperature ensemble (NVT). The temperature is controlled via Nosè-Hoover chains thermostat[92].

Trajectory analysis was performed to investigate the intrinsic mobility of the polymer systems as a function of the cross-linking ratio. The radius of gyration (R_g) was used to assess the structural stability of the polymers and was computed using the internal routines of VMD software. The square of the radius of gyration is defined as

$$R_g^2(r) = \frac{\sum_i m_i (r_i - r_{CoM})^2}{\sum_i m_i} \quad (6).$$

The solvent-accessible surface area (SASA) was used to probe differences in polymer mobility and surface roughness at the polymer–vacuum interface. SASA calculations were performed using the FreeSASA library[93] via a custom Python script, which allowed the analysis to be restricted to the external surfaces exposed to vacuum along the x-y plane. A probe radius of 1.4 Å, corresponding to the approximate size of a water molecule, was adopted.

Density Functional Theory calculations. Three representative configurations were extracted from the MD simulations for DFT calculations (see Fig. S13 for a visual representation of the three optimized polymer slabs). All slab configurations share the same lateral dimensions in the x-y plane (20x20 Å²), while the cell length along the *z* direction was reduced to 45 Å to limit the computational cost of geometry optimization. Nevertheless, a vacuum region of at least 15 Å was maintained along the *z* direction in all systems to avoid spurious interactions.

Geometric optimizations of polymers were performed within Density Functional Theory (DFT) using the PBE exchange-correlation functional and the Projector-Augmented Wave (PAW) method[94], as implemented in the VASP program[95-99]. Van der Waals interactions were accounted for using the DFT-D3 method with Becke–Johnson damping[100]. A plane-wave kinetic energy cutoff of 520 eV was employed.

The work function, F, is computed using the following expression:

$$\Phi = e\phi_{vacuum} - \varepsilon_F \quad (7)$$

where F_{vacuum} is the vacuum potential (the potential sufficiently far away from the surface that an electron there do not feel the presence of the surface), e is the charge of electron, and e_F is the Fermi level of the surface. After reaching the geometric convergence, a final single point calculations were employed to obtain the above quantities.

Data availability

The data supporting the findings of this study are available in the main text and Supplementary Information, or available from the corresponding author upon reasonable request.

References

1. Shen, Y. *et al*. An experimental study of triboelectrostatic particle charging behavior and its associated fundamentals. *Powder Technol*. **429**, 118880 (2023).
2. Bhaduri, A. & Ha, T.-J. Biowaste-derived triboelectric nanogenerators for emerging bioelectronics. *Adv. Sci*. **11**, 2405666 (2024).
3. Kopp, S.-P. *et al*. Enabling triboelectric charging as a powder charging method for electrophotographic powder application in laser-based powder bed fusion of polymers by triboelectric charge control. *Addit. Manuf*. **68**, 103531 (2023).
4. Pal, A. *et al*. Construction of triboelectric series and chirality detection of amino acids using triboelectric nanogenerator. *Adv. Sci*. **11**, 2307266 (2024).
5. Zhao, J. *et al*. Enhanced electrocatalytic synthesis and degradation enabled by triboelectric effect. *Nano Energy* **139**, 110962 (2025).
6. Verners, O. *et al*. Smooth polymers charge negatively: controlling contact electrification polarity in polymers. *Nano Energy* **104**, 107914 (2022).
7. Sherell, P. C. *et al*. Probing contact electrification: a cohesive sticky problem. *ACS Appl. Mater. Interfaces*. **13**, 44935–44947 (2021).
8. Lapčinskis, L. *et al*. The adhesion-enhanced contact electrification and efficiency of triboelectric nanogenerators. *Macromol. Mater. Eng*. **305**, 1900638 (2020).
9. Ģērmane, L. *et al*. Physical and chemical surface modification of recycled polystyrene films for improved triboelectric properties. *Energy Technol*. **12**, 2400762 (2024).
10. Ghori, M. U., Šupuk, E. & Conway, B. R. Tribo-electrification and powder adhesion studies in the development of polymeric hydrophilic drug matrices. *Materials* **8**, 1482–1498 (2015).
11. Pandey, R. K., Kakehashi, H., Nakanishi, H. & Soh, S. Correlating material transfer and charge transfer in contact electrification. *J. Phys. Chem. C*. **122**, 16154–16160 (2018).
12. Šutka, A. *et al*. Engineering polymer interfaces: a review toward controlling triboelectric surface charge. *Adv. Mater. Interfaces*. **10**, 2300323 (2023).
13. Jabbari, E. & Peppas, N. A. Polymer-polymer interdiffusion and adhesion. *J. Macromol. Sci., Polym. Rev*. **34**, 205–241 (1994).
14. Maeda, N., Chen, N., Tirrell, M. & Israelachvili J. N. Adhesion and friction mechanisms of polymer-on-polymer surfaces. *Science* **297**, 379–382 (2002).
15. Šutka, A. *et al*. The role of intermolecular forces in contact electrification on polymer surfaces and triboelectric nanogenerators. *Energy Environ. Sci*. **12**, 2417-2421 (2019).
16. Li, X. *et al*. Harnessing triboiontronic Maxwell's demon by triboelectric-induced polarization for efficient energy-information flow. *Joule* **9**, 101888 (2025).
17. Li, X., Li. R., Li. S., Wang, Z. L., & Wei, D. Triboiontronics with temporal control of electrical double layer formation. *Nat. Commun*. **15**, 6182 (2024).

18. Li, X., Wang, Z. L., & Wei, D. Scavenging energy and information through dynamically regulating the electrical double layer. *Adv. Funct. Mater*. **34**, 2405520 (2024).
19. Li, X. *et al*. Triboiontronics for efficient energy and information flow. *Matter* **6**, 3912-3926 (2023).
20. Jimidar, I. S. M. *et al*. Influence of wettability and geometry on contact electrification between nonionic insulators. *ACS Appl. Mater. Interfaces*. **15**, 42004–42014 (2023).
21. McCarty, L. S. & Whitesides, G. M. Electrostatic charging due to separation of ions at interfaces: Contact electrification of ionic electrets. *Angew. Chem., Int. Ed*. **47**, 2188–2207 (2008).
22. Varner, H. & Cohen, T. Explaining the spread in measurement of PDMS elastic properties: influence of test method and curing protocol. *Soft Matter* **20**, 9174–9183 (2024).
23. Sales, F. C.P., Ariati, R. M., Noronha, V. T. & Ribeiro, J. E. Mechanical characterization of PDMS with different mixing ratios. *Procedia Structural Integrity* **37**, 383–388 (2022).
24. Babu, A. R. & Gundiah, N. Contributions of network topological structures to the mechanical properties of PDMS elastomers. *Mater. Res. Express*. **5**, 085310 (2018).
25. Niamlang, S. & Sirivat, A. Electromechanical responses of a crosslinked polydimethylsiloxane. *Macromol. Symp*. **264**, 176–183 (2008).
26. Chano, K., Poliskie, G. M. & Fregoso, J. Rheology of thermal interface materials composed of silicone gels. *IEEE Trans. Compon., Packag., Manuf. Technol*. **7**, 217 – 220 (2017).
27. Valentin, J. D. P. *et al*. Substrate viscosity plays an important role in bacterial adhesion under fluid flow. *J. Colloid Interface Sci*. **552**, 247–257 (2019).
28. Cai, C. *et al*. Enhanced electromechanical properties of three-phased polydimethylsiloxane nanocomposites via surface encapsulation of barium titanate and multiwalled carbon nanotube with polydopamine. *Macromol. Mater. Eng*. **306**, 2100046 (2021).
29. Sakasegawa, D. *et al*. Effects of degree of cross-links on adhesion curves of cross-linked polymers observed by a point-contact method. *Langmuir* **26**, 5856–5863 (2010).
30. Bistac, S., Galliano, A. & Schmitt, M. Nanofriction of polymers: the complex role of adhesion. *J. Phys.: Condensed Matter*. **20**, 354015 (2008).
31. Dorogin, L. & Persson, B. N. J. Contact mechanics for polydimethylsiloxane: from liquid to solid. *Soft Matter*. **14**, 1142–1148 (2018).
32. Li, Z., Yu, H. & Wang, J. Contact creep behavior of polydimethylsiloxane and influence of load, tip size, and crosslink density. *Tribol. Lett*. **49**, 291–299 (2013).
33. Cai, J.-H., Huang, M.-L., Chen, X.-D. & Wang, M. Controllable construction of cross-linking network for regulating on the mechanical properties of polydimethylsiloxane and polydimethylsiloxane/carbon nanotubes composites. *J. Appl. Polym. Sci*. **139**, 52113 (2022).
34. Qian, S. *et al*. The viscoelastic response of soft material: A theoretical and experimental study based on barreling deformation. *Polym. Test*. **70**, 474–480 (2018).
35. Bunk, J. K. G. *et al*. Studying the influence of chemical structure on the surface properties of polymer films. *Colloids Surf., A*. **362**, 47–57 (2010).

36. Németh, E., Albrecht, V., Schubert, G. & Simon, F. Polymer tribo-electric charging: dependence on thermodynamic surface properties and relative humidity. *J. Electrost*. **58**, 3–16 (2003).
37. Li, S. *et al*. Contributions of different functional groups to contact electrification of polymers. *Adv. Mater*. **32**, 2001307 (2020).
38. Johnson, L. M. *et al*. Elastomeric microparticles for acoustic mediated bioseparations. *J. Nanobiotechnol*. **11**, 22 (2013).
39. Nakamura, K. & Ichimura, S. Vibrational spectroscopic study of the interface of SiO_2/Si(100) fabricated by highly concentrated ozone: Direct evidence for less strained Si–O–Si bond angle. *Jpn. J. Appl. Phys*. **44**, 7602 (2005).
40. Alexandru, M. Siloxane-organic networks in *Recent developments in silicone-based materials* (ed. Cazacu, M.) 107–133 (Nova Science Publishers, Inc., 2010).
41. Li, R. *et al*. Robustly curing epoxy novolacs by linear and cyclic siloxane-functionalized eugenol: Impact of topologies of cross-linkers on properties of thermosets. *ACS Appl. Mater*. **6**, 756–767 (2024).
42. Wójcik-Bania, M. Influence of the addition of organo-montmorillonite nanofiller on cross-linking of polysiloxanes – FTIR studies. *Spectrochim. Acta, Part A*. **252**, 119491 (2021).
43. Lisensky, G. C. *et al*. Replication and compression of surface structures with polydimethylsiloxane elastomer. *J. Chem. Educ*. **76**, 537 (1999).
44. Cho, H. S., Moon, H.-Y., Lee, H. S., Kim, Y. T. & Jeoung, S. C. Formulation prediction for Young's modulus of poly(dimethylsiloxane) by spectroscopic methods. *Bull. Korean Chem. Soc*. **42**, 1225–1231 (2021).
45. Borjanović, V. *et al*. Influence of proton irradiation on the structure and stability of poly(dimethylsiloxane) and poly(dimethylsiloxane)-nanodiamond composite. *J. Vac. Sci. Technol. B*. **27**, 2396–2403 (2009).
46. Roychowdhury, T., Cushman, C. V., Synowicki, R. A. & Linford, M. R. Polydimethylsiloxane: Optical properties from 1991 to 1688 nm (0.735–6.49 eV) of the liquid material by spectroscopic ellipsometry. *Surf. Sci. Spectra*. **25**, 026001 (2018).
47. Bae, S. C., Lee, H., Lin, Z. & Granick, S. Chemical imaging in a surface forces apparatus: Confocal Raman spectroscopy of confined poly(dimethylsiloxane). *Langmuir* **21**, 5685–5688 (2005).
48. Fu, H. *et al*. Understanding contact electrification via direct covalent bond cleavage of polymer chains for ultrahigh electrostatic charge density. *Energy Environ. Sci*. **17**, 3776–3787 (2024).
49. Fang, Y. *et al*. Static charge is an ionic molecular fragment. *Nat. Commun*. **15**, 1986 (2024).
50. Lee, D. W. *et al*. Correlation between frictional heat and triboelectric charge: In operando temperature measurement during metal-polymer physical contact. *Nano Energy* **103**, 107813 (2022).
51. Ye, J. *et al*. Functionalized PDMS for regulating the triboelectric output of nanogenerators: a study of charge transfer mechanisms. *J. Mater. Chem. C*. **13**, 7654–7663 (2025).

52. Baytekin, B., Baytekin H. T. & Gryzbowski, B. A. What really drives chemical reactions on contact charged surfaces? *J. Am. Chem. Soc*. **134**, 7223–7226 (2012).
53. Sakaguchi, M., Makino, M., Ohura, T. & Iwata, T. Contact electrification of polymers due to electron transfer among mechano anions, mechano cations and mechano radicals. *J. Electrost*. **7**, 412–416 (2014).
54. Baytekin, H. T., Baytekin, B., Incorvati, J. T. & Gryzbowski, B. A. Material transfer and polarity reversal in contact charging. *Angew. Chem., Int. Ed*. **51**, 4843 – 4847 (2012).
55. Puhan, D. & Wong, J. S. S. Properties of polyetheretherketone (PEEK) transferred materials in a PEEK-steel contact. *Tribol. Int*. **135**, 189–199 (2019).
56. Yang, P. *et al*. Radical anion transfer during contact electrification and its compensation for charge loss in triboelectric nanogenerator. *Matter* **6**, 1295–1311 (2023).
57. Ghatak, A., Vorvolakos, K., She, H., Malotky, D. L. & Chaudhury, M. K. Interfacial rate processes in adhesion and friction. *J. Phys. Chem. B*. **104**, 4018–4030 (2000).
58. Kleyman, G., Kang, T., Twiefel, Jens & Voit, W. Characterization of triboelectric charge generation between PTFE and nylon after repeated contacts. *Energy Harvesting and Systems* **4**, 165–176 (2017).
59. Wu, J., Zhu, W., Wen, Q., Cao, J. & Cao, Q. Effect of contact electrification on the adhesion behavior of copper/polydimethylsiloxane interface: an atomic-scale investigation. *Appl. Surf. Sci*. **704**, 163397 (2025).
60. Ģērmane, L., Lapčinskis, L., Iesalnieks, M. & Šutka, A. Surface engineering of PDMS for improved triboelectrification. *Mater. Adv*. **4**, 875–880 (2023).
61. Zhang, R. *et al*. All-inorganic triboelectric nanogenerators based on $Mo_6S_3I_6$ and indium tin oxide. *Nano Energy* **89**, 106363 (2021).
62. Pal, D. & Neogi, S. Enhancement of adhesion of polymers by plasma treatment in *Progress in Adhesion and Adhesives* (ed. Mittal, K. L.) 65–108 (Scrivener Publishing LLC, 2025).
63. Ohkubo, Y. *et al*. Drastic improvement in adhesion property of polytetrafluoroethylene (PTFE) via heat-assisted plasma treatment using a heater. *Sci. Rep*. **7**, 9476 (2017).
64. Haartsen, S. *et al*. Tailoring the adhesion properties of thin polymeric films using additives: an AFM study. *Nanoscale Adv*. **8**, 1273–1280 (2026).
65. Bao, C. *et al*. Cross-linking the surface of cured polydimethylsiloxane via hyperthemal hydrogen projectile bombardment. *ACS Appl. Mater. Interfaces* **7**, 8515–8524 (2015).
66. Lowell, J. Bidirectional charge transfer in repeated contacts to polymers. J. *Electrost*. **20**, 233–238 (1987).
67. Baytekin, H. T. *et al*. The mosaic of surface charge in contact electrification. *Science* **333**, 308 – 312 (2011).
68. Pertl, F., Lenton, I. C. D., Cramer, T. & Waitukaitis, S. No time for surface charge: How bulk conductivity hides charge patterns from Kelvin probe force microscopy in contact-electrified surfaces. *Phys. Rev. Lett*. **135**, 146202 (2025).

69. Sobolev, Y. I., Adamkiewicz, W., Siek, M. & Grzybowski, B. A. Charge mosaics on contact-electrified dielectrics result from polarity-inverting discharges. *Nat. Phys*. **18**, 1347–1355 (2022).
70. Zhang, H., Sundaresan, S. & Webb. M. A. Thermodynamic driving forces in contact electrification between polymeric materials. *Nat. Commun*. **15**, 2616 (2024).
71. Li, Y. *et al*. Visualization and standardized quantification of surface charge density fro triboelectric materials. *Nat. Commun*. **15**, 6004 (2024).
72. Musa, U. G., Cezan, S. D., Baytekin, B. & Baytekin, H. T. The charging events in contact-separation electrification. *Sci. Rep*. **8**, 2472 (2018).
73. Burgo, T. A. L., Batista, B. C. & Galembeck, F. Electricity on rubber surfaces: a new energy conversion effect. *ACS Omega* **2**, 8940–8947 (2017).
74. Wattanasarn, H., Ngennam, T., Sumpao, T., Thanachayanont, C. & Seetwawan, T. The charging performance in contact electrification of fluorinated ethylene propylene surfaces by electrode bridge. *Sens. Actuators, A*. **346**, 113881 (2022).
75. Liu, Y. et al. Enhancement of triboelectric charge density by chemical functionalization. *Adv. Funct. Mater*. **30**, 2004714 (2020).
76. Huang, P. – R., He, Y., Cao, C. & Lu, Z. – H. The origin of the high work function of chlorinated indium tin oxide. *NPG Asia Mater*. **5**, e57 (2013).
77. Bal-Ozturk, A. *et al*. Tissue adhesives: from research to clinical translation. *Nano Today* **36**, 101049 (2021).
78. Lee, J. H. & Lee, D. W. Contact-induced molecular rearrangement of acrylic acid-incorporated pressure sensitive adhesives. *Appl. Surf. Sci*. **500**, 144246 (2020).
79. Li, M. *et al*. Effects of bulk viscoelasticity and surface wetting on the contact and adhesive properties of a soft material. *Polym. Test*. **74**, 266–273 (2019).
80. Martina, D., Creton, C., Damman, P., Jeusette, M. & Lindner, A. Adhesion of soft viscoelastic adhesives on periodic rough surfaces. *Soft Matter* **8**, 5350–5357 (2012).
81. Zhang, J. *et al*. Irreproducibility in the triboelectric charging of insulators: evidence of a non-monotonic charge versus contact time relationship. *Phys. Chem. Chem. Phys*. **22**, 11671–11677 (2020).
82. Yan, W. *et al*. Contact enhancement effect: Extending the duration of contact state to enhance the output of contact-separation triboelectric nanogenerators. *Mater. Today Comun*. **43**, 111686 (2025).
83. Lamberti, A., Donato, M. D., Chiappone, A., Giorgis, F. & Canavese, G. Tunable electromechanical actuation in silicone dielectric film. *Smart Mater. Struct*. **23**, 105001 (2014).
84. Moučka, R., Sedlačík, M., Osička, J. & Pata, V. Mechanical properties of bulk Sylgard 184 and its extension with silicone oil. *Sci. Rep*. **11**, 19090 (2021).
85. Cho, H. S., Moon, H.–Y., Lee, H. S., Kim, Y. T. & Jeoung, S. C. Formulation prediction for Young's modulus of poly(dimethylsiloxane) by spectroscopic methods. *Bull. Korean Chem. Soc*. **42**, 1225–1231 (2021).

86. Kong, D., Meng, Y. & McKenna, G. B. Determination of the molecular weight between cross-links for different ambers: viscoelastic measurements of the rubbery plateau. *Polym. Eng. Sci*. **62**, 1023–1040 (2022).
87. Johnson, K. L., Kendall, K. & Roberts, A. D. Surface energy and the contact of elastic solids. *Proc. A* **324**, 301–313 (1971).
88. Thompson, A. P. *et al*. LAMMPS – a flexible simulation tool for particle-based materials modeling at the atomic, meso, and continuum scales. *Comput. Phys. Commun*. **271**, 108171 (2022).
89. Mayo, S. L., Olafson, B. D. & Goddard, W. A. DREIDING: a generic force field for molecular simulations. *J. Phys. Chem*. **94**, 8897–8909 (1990).
90. Sasaki, K. & Yamashita, T. Modification and validation of the DREIDING force field for molecular liquid simulations (DREIDING-UT). *J. Chem. Inf. Model*. **61**, 1172–1179 (2021).
91. Xiang, Z. *et al*. Force-field benchmark for polydimethylsiloxane: Density, heat capacity, isothermal compressibility, viscosity and thermal conductivity. *J. Phys. Chem. B* **129**, 1864–1873 (2025).
92. Martyna, G. L., Klein, M. L. & Tuckerman, M. Nosé-Hoover chains: The canonical ensemble via continuous dynamics. *J. Chem. Phys*. **97**, 2635–2643 (1992).
93. Mitternacht, S. FreeSASA: An open source C library for solvent accesible surface area calculations [version 1; peer review: 2 approved]. *F1000Research* **5**, 189 (2016).
94. Blöchl, P. E. Projector augmented-wave method. *Phys. Rev. B* **50**, 17593 (1994).
95. Kresse, G. & Hafner, J. Ab initio molecular-dynamics simulation of the liquid-metal-amorphous-semiconductor transition in germanium. *Phys. Rev. B* **49**, 14251 (1994).
96. Kresse, G. & Hafner, J. Ab initio molecular dynamics for liquid metals. *Phys. Rev. B* **47**, 558 (1993).
97. Kresse, G. & Furthmüller, J. Efficiency of ab-initio total energy calculations for metals and semiconductors using a plane-wave basis set. *Comput. Mater. Sci*. **6**, 15–50 (1996).
98. Kresse, G. & Furthmüller, J. Efficient iterative schemes for ab initio total-energy calculations using a plane-wave basis set. *Phys. Rev. B* **54**, 11169 (1996).
99. Kresse, G. & Hafner, J. Norm-conserving and ultrasoft pseudopotentials for first-row and transition elements. *J. Phys.: Condens. Matter* **6**, 8245 (1994).
100. Grimme, S., Ehrlich, S. & Goerigk, L. Effect of the damping function in dispersion corrected density functional theory. *J. Comput. Chem*. **32**, 1456–1465 (2011).

Acknowledgements

Līva Ģērmane acknowledges the support by the EU Recovery and Resilience Facility within Project No. 5.2.1.1.i.0/2/24/I/CFLA/003 “Implementation of consolidation and management

changes at Riga Technical University, Liepaja University, Rezekne Academy of Technology, Latvian Maritime Academy and Liepaja Maritime College for the progress towards excellence in higher education, science and innovation" academic career doctoral grant (ID 1031). Andrea Le Donne acknowledges ISCRA for awarding this project access to the LEONARDO supercomputer, owned by the EuroHPC Joint Undertaking, hosted by CINECA (Italy). Jiahao Ye acknowledges support from the UKRI Engineering and Physical Sciences Research Council (EPSRC) under Grant No. TEGMOF EP/Z534146/1." The authors thank Anna Šutka for her assistance with visual formatting.

Author contributions

Līva Ģērmane: methodology, investigation, formal analysis, data curation, visualization, funding acquisition. Linards Lapčinskis: formal analysis, supervision, conceptualization. Tianhuai Xu, Jiahao Ye, Hermanis Sorokins and Jēkabs Grušss: investigation. Andrea Le Donne: investigation and formal analysis. Jin-Chong Tan and Andris Šutka: conceptualization and supervision. Writing – original draft was equally contributed by all the authors.

Competing interests

The authors declare no competing interests.

Editorial Summary:

The role charge magnitude on triboelectrification depends on surface chemistry, morphology, and mechanical properties, yet the role of adhesion remains unclear. Here, PDMS films with different base polymer-to-curing agent ratios yields distinct viscoelastic and adhesive properties without altering chemical structure.

Peer review information:

Communications Materials thanks Galien Grosjean, Alireza Akbarinejad and the other, anonymous, reviewer(s) for their contribution to the peer review of this work. A peer review file is available.